Available online at www.sciencedirect.com
SCIENCE DIRECT®
Physics of the Earth and Planetary Interiors 135 (2003) 137–159
PHYSICS OF THE EARTH AND PLANETARY INTERIORS
www.elsevier.com/locate/pepi

Lorentz force effects in magneto-turbulence

Daniel R. Sisan, Woodrow L. Shew, Daniel P. Lathrop*

Department of Physics, IREAP and IPST, University of Maryland, College Park, MD 20742, USA

Received 6 December 2001; received in revised form 12 July 2002; accepted 25 September 2002

Abstract

We experimentally characterize magnetic field fluctuations in a strongly turbulent flow of liquid sodium in the presence of a large externally applied field. We reach high interaction parameter (up to $N = 17$) for moderate magnetic Reynolds number (up to $Re_m = 18$), a previously unexplored parameter range for liquid metal flows. As the interaction parameter (i.e. the ratio of Lorentz to inertial forces) is increased, the system passes through distinct regimes, which we classify. We find that for certain ranges of the applied magnetic field, particularly at high values, the induced magnetic field exhibits large, coherent oscillations. Spatial structure in these induced field oscillations suggests the formation of non-axisymmetric vortices that precess at a fraction of the impeller rotation rate. We also investigate the effect of rough versus smooth boundaries and relate these results to topographic core–mantle coupling in the Earth.

PACS: 47.27.Jv; 47.65.+a; 98.38.Am; 91.25.Cw

Keywords: Dynamo; Geodynamo; MHD turbulence; Interaction parameter; Magnetic Reynolds number

1. Introduction

There is extensive research indicating that planetary magnetic fields arise from flowing electrically-conducting fluids. Since the 1960s, many researchers have found self-generating dynamo solutions of the governing equations for the magnetic field and fluid motion (Steenbeck et al., 1966; Moffatt, 1978; Dudley and James, 1989). More recently, numerical research has shown dynamo action, including field reversals and more complicated dynamics, in approximately realistic simulations of the Earth's core (Glatzmaier and Roberts, 1995; Kuang and Bloxham, 1997). Dormy et al. (2000), and Roberts and Glatzmaier (2000), present excellent reviews. Recently, groups in Riga, Latvia (Gailitis et al., 2000, 2001) and Karlsruhe, Germany (Stieglitz and Müller, 2001) have produced liquid metal laboratory dynamos, in geometries that force helical flow using baffling and duct-work. A logical next step is producing a laboratory dynamo in a geometry where Lorentz forces can greatly modify the velocity field. A number of groups including our own are attempting this (Odier et al., 1998; Beckley et al., 1998; O'Connell et al., 2001; Peffley et al., 2000).

Experimentally studying the interaction of magnetic fields and electrically-conducting flows has the potential to answer a number of open questions. First is the effect of turbulence, which experiments are well suited to study. In the Earth's core, turbulence most likely has a significant effect on the Earth's field, as best evidenced by the broad magnetic energy spectra at the core–mantle boundary. Satellite data imply

* Corresponding author.
E-mail address: dpl@complex.umd.edu (D.P. Lathrop).

0031-9201/03/$ – see front matter © 2003 Elsevier Science B.V. All rights reserved.
doi:10.1016/S0031-9201(02)00212-1

that the Earth's field at the core–mantle boundary has significant contributions at least up to degree $l = 12$ (Hulot et al., 2002). As the Earth's mantle filters the field increasingly with higher l, the Earth's field may thus be even more broadband than we are able to infer from the surface. Evidence that turbulence is significant is also found in experiments (Odier et al., 1998; Peffley et al., 2000).

Other approaches to the dynamo problem may miss important effects of turbulence. In theoretical studies, turbulence is either treated using approximations and parameterizations, e.g. the α- and β-effects, or only stationary flows are considered. In numerical work, hyperdiffusivities or an artificially large magnetic Prandtl number (e.g. setting the ratio of the kinematic viscosity to the magnetic diffusivity, $Pr_m \equiv \nu/\eta$, to order unity—whereas $Pr_m \sim 10^{-6}$ for the Earth's core (Dormy et al., 2000)) purposefully limit turbulence. In the Riga and Karlsruhe experiments, turbulence does not play a direct role in the magnetic field dynamics. For instance, the Karlsruhe dynamo is two-scale: while the velocity field is small-scale and turbulent, the magnetic field is large scale and apparently only slightly affected by the fluid turbulence.

Furthermore, in the Riga and Karlsruhe experiments the magnetic field reaches equilibrium through mechanisms that are different than those operating in planetary core dynamos. In the Karlsruhe experiment, the equilibrium magnetic energy corresponds simply to the pressure head in excess of the critical value for dynamo action. In a less constrained dynamo, on the other hand, the equilibrium magnetic energy would be much harder to predict as Lorentz forces would alter the flow in a more complicated way. A recent paper by Gailitis et al. (2001) showed evidence of saturation in the Riga dynamo experiment that appears more complicated than the saturation in the Karlsruhe experiment. However, the saturated field value was small (8 G) for moderate magnetic Reynolds number, corresponding to an interaction parameter much less than one, far from the regime thought present in the Earth. Although we have not produced a self-generating dynamo like the experiments in Karlsruhe and Riga, we are nonetheless closer to the parameter range where the Earth's dynamo is thought to operate. For a more extensive discussion of the relation between dynamo theory and experiments see a review by Busse (2000).

Previous liquid metal experiments attempting to produce dynamos in unconstrained flows used small external applied fields (Odier et al., 1998; Peffley et al., 2000). The applied fields there were used to probe the system in two ways. In one, induced fields were measured, which result from twisting and shearing of a constant field by the conducting fluid. In the other, the decay of a pulsed applied field probed how close the system was to self-generation. Small fields were desirable for these purposes so that Lorentz forces did not alter the flow.

In this study, the applied fields are purposefully large enough to alter the flow. In other words, the interaction parameter, the ratio of the Lorentz to inertial forces, is made greater than unity. The interaction parameter is $N = B^2 L/\rho\mu_0\eta U$, where B is the magnetic field, U and L the characteristic velocity and length scales, ρ the density, and μ_0 the magnetic permeability. Near unity interaction parameter should be an interesting regime, as a competition exists between two dominant forces. Although the interaction parameter in the Earth is much greater than one, there is a length scale within the outer core where N is comparable to our experiments. One place where structures at these length scales might be especially important is in the outer core boundary layers. The boundary layers may play a crucial role in the global state of the outer core, and specifically in the magnetic field saturation.

In addition to a force balance, turbulence, or its suppression by the magnetic field, could affect saturation of the magnetic field. For instance, in the Earth's core small-scale currents (due to small-scale turbulent velocity fluctuations) could contribute to Joule heat production, even if they do not contribute directly to the observable field. Joule heat production, which obviously cannot exceed the power source driving the dynamo, places limitations on the intensity of magnetic fields in the core. Brito et al. (1996) studied Joule heating in turbulent gallium flows for a range of applied fields and found that the fields had a significant effect. As the applied field was increased for a fixed rotation rate, Joule heating increased and then decreased, similar to some of our observations. However, their magnetic Reynolds number and interaction parameter (as defined here) were less than one. Although we do not directly measure Joule heating in our experiments, the sudden change in dynamics

we observe at large interaction parameter could make extrapolating from Brito's study to higher interaction parameter problematic. It should be noted, however, that our applied field direction is parallel to the rotation axis, whereas Brito's was transverse.

Many other experimental studies of magnetic fields on electrically-conducting flows (Rayleigh–Benard convection, duct flows, magnetically-driven flows, flow around obstacles, etc.) have been performed (Moreau, 1990; Brito et al., 1995). However, to our knowledge, no experiments have been performed for high N, $Re_m = UL/\eta > 1$.

Lastly, our experiment relates to a paper by Hollerbach and Skinner (2001). They studied, numerically, spherical Couette flow with large applied fields parallel to the axis of rotation. The applied fields induced instabilities in their system that resemble in many ways the dynamics in our experiment. They can only reach Reynolds numbers $Re = Re_m/Pr_m \sim O(10^3)$, however, and the system changes significantly past the critical value for the instabilities. Thus our experiment, with its range of much larger Reynolds numbers $Re \sim O(10^6)$ and similar geometry, significantly extends their result.

In this paper, we present magnetic field and torque measurements taken over a range of interaction parameter. These data exhibit phenomena that depend mainly on the interaction parameter (and weakly on Re_m)—suppression of turbulence, regular oscillations in the induced magnetic field, and spatial correlations with complex structure. We also find that angular momentum transfer between the fluid and the spherical vessel depends in rather unexpected ways on the applied field and topography of the vessel. We demonstrate that the interaction parameter is the relevant parameter describing these phenomena, and we classify the major regimes. Finally, we make an interpretation of the flow dynamics and discuss implications for the dynamics in the Earth's core.

2. The experiment

The liquid sodium is contained in a 31.2 cm hollow sphere of 304 (nonmagnetic) stainless steel. The flow is driven by two 12.7 cm diameter titanium impellers on 2.5 cm diameter shafts entering the sphere from either pole (see Fig. 1). Each shaft is belt-driven by a 7.5 kW electric motor. The results we report in this paper are for co-rotating impellers.

Table 1
Important dimensional parameters for the experiment and sodium at 120 °C

Symbol	Description	Value
b	Impeller radius (cm)	6.35
a	Sphere radius (cm)	15.6
η	Sodium magnetic diffusivity (cm^2/s)	830
ν	Sodium kinematic viscosity (cm^2/s)	7.39×10^{-3}
ρ	Sodium density (g/cm^3)	0.927

Two coils in near-Helmholtz configuration supply the external field concentric to the axis of impeller rotation. The applied field varies approximately 10% from the center of the sphere to the outer edge. The applied field decreases away from the center along the axis of rotation, and increases in the other two perpendicular directions. Magnetic fields are monitored with Hall probes near the sphere. Three Hall arrays were used: a 15 cm diameter ring (six probes) encircling one pole azimuthally, a pole-to-pole arc (eight probes), and an equatorial arc (seven probes) all of which measure fields perpendicular to the applied field (see Fig. 1). The equatorial array is augmented by two single Hall probes, one of which is offset slightly from the equator. A Hall probe just outside the sphere next to one shaft measured the field in the direction parallel to the applied field. Table 1 shows relevant experimental parameters for our system. More detail regarding the experimental apparatus can be found in Peffley et al. (2000).

We perform experiments both with baffles and with smooth walls. The baffles are thin stainless steel plates that run from pole to equator in each hemisphere. They extend 5% of the sphere diameter. These baffles increase the ratio of poloidal to toroidal flow, as originally motivated by Dudley and James's study (1989) of simple velocity fields in a spherical geometry and their ability to self-generate. We found in Peffley et al. (2000) that a trend toward self-generation using pulse decay measurement was only possible with these baffles in place. In this experiment, the baffles' role is to create topographic variation at the vessel wall, analogous to topographic variation at the Earth's core–mantle boundary.

Experimental runs were performed using the following procedure. The impellers were spun at a fixed

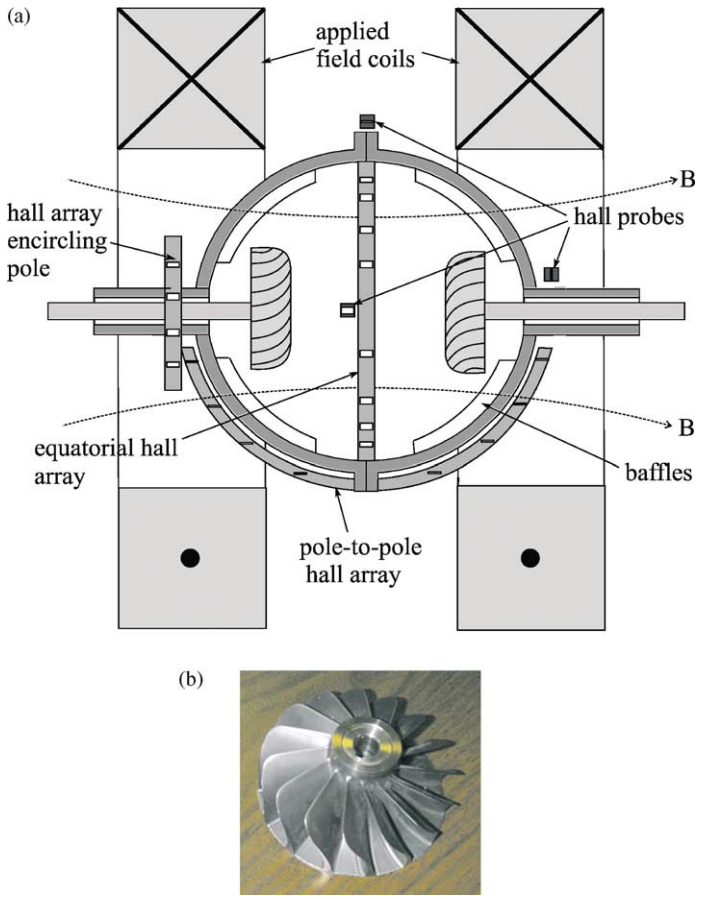

Fig. 1. Schematic of experimental apparatus showing the spherical vessel and impellers, pole-to-pole baffles, coils supplying the external field, Hall probes, and Hall arrays (a pole-to-pole arc, a 15 cm diameter ring encircling one pole, and an equatorial arc). (b) shows a photograph of the impellers. The two impellers have the same shape. The single Hall probe shown in the center of the figure is slightly offset from the equatorial array outside the sphere. The array encircling one pole nearly touches the sphere (approximately 5 cm from the sodium). All Hall probes measure the field perpendicular to the applied field, except for the probe at the pole (opposite the array encircling one pole). Runs were performed with and without the baffles.

rotation rate, and the field was incrementally increased through its full range. The maximum field obtainable was 2×10^3 G. However, the magnets heated throughout the day and thus lowered the maximum obtainable field value. For each field value, data were taken for several seconds (typically 4 or 16 s).

3. Equations of motion

The dimensionless equations of motion relevant to our system are the Navier–Stokes equation with the added Lorentz force:

$$\frac{\partial \vec{u}}{\partial t} + (\vec{u} \cdot \vec{\nabla})\vec{u} = -\vec{\nabla} P + Re^{-1}\nabla^2 \vec{u} + N\, Re_{\mathrm{m}}^{-1}(\vec{\nabla} \times \vec{B}) \times \vec{B} \quad (1)$$

and the induction equation:

$$\frac{\partial \vec{B}}{\partial t} = \vec{\nabla} \times \vec{u} \times \vec{B} + Re_{\mathrm{m}}^{-1}\nabla^2 \vec{B} \quad (2)$$

derived from Maxwell's equations and Ohm's law for a moving conductor, where $\vec{u}$ is the velocity, P the pressure, and $\vec{B}$ the magnetic field. The dimensionless

Table 2
Relevant dimensionless parameters

	Dimensionless parameter		
	Re	Re_m	N
Definition	UL/ν	UL/η	$B^2L/U\eta\rho\mu_0$
Range for experiment	5×10^5 to 4×10^6	3.8–18	0–17
Estimate for Earth	$\sim10^8$	~100	$\sim10^5$–10^7
Estimate for Sun	$\sim10^2$–10^{11}	$\sim10^2$–10^4	~1–10^4

Parameter estimates for the Earth use the westward drift rate of field patterns ($U\approx10^{-4}$ m/s) for the velocity and $B=5$ G (radial component at core-mantle boundary) to $B=500$ G (estimated toroidal component) for the magnetic field. Density, electrical conductivity, kinematic viscosity, and length scale of the fluid core are taken from Roberts (1988). Estimates for the Sun are discussed in Section 5.2.

parameters; the Reynolds number $Re = UL/\nu$, the magnetic Reynolds number Re_m, and the interaction parameter N are described in Table 2 and the next section. In the equations above, the velocity $\vec{u}$ has been scaled by the impeller tip speed Ωb, time by the rotational time scale Ω^{-1}, length by the sphere radius a, and the magnetic field $\vec{B}$ by the imposed field strength B_0 (Table 2) .

In addition, sodium is effectively incompressible in these conditions:

$$\vec{\nabla}\cdot\vec{u}=0. \tag{3}$$

No-slip boundary conditions for the velocity apply at all surfaces. The magnetic field boundary condition is approximately continuous with an exterior vacuum solution, as stainless steel is a poor electrical conductor.

3.1. Dimensionless parameters

The state of the fluid flow, and thus the induced field, depends on a competition between the inertial and Lorentz forces (the second and fifth terms in Eq. (1)). The interaction parameter quantifies the competition. An expression for the interaction parameter can be found using dimensional analysis. Using Ohm's law $\vec{J}=\sigma(\vec{E}+\vec{u}\times\vec{B})$ (where σ is the electrical conductivity, and $\vec{E}$ the electric field) and a scaling from Faraday's law ($E_{ind}\sim uB_{ind}$), the dimensional form of the Lorentz force per unit mass ($\vec{F}=\vec{J}\times\vec{B}/\rho$) scales as:

$$F_{Lor}\sim\frac{\sigma}{\rho}uB_{ext}B_{ind}+\frac{\sigma}{\rho}uB_{ext}^2 \tag{4}$$

where ρ is the density. The induced magnetic field is about 1000 times smaller than the external magnetic field in our experiments, so the second term above dominates.

Since the advective term in the Navier–Stokes equation scales as U^2/L, where L is a characteristic length, the interaction parameter can be expressed as $N=B_{ext}^2L/\eta\rho\mu_0u$, where $\eta\equiv1/\sigma\mu_0$ is the magnetic diffusivity, composed of the electrical conductivity and magnetic permeability. Using the sphere radius a, and the impeller tip speed Ωb, gives

$$N=\frac{B_{ext}^2a}{\eta\rho\mu_0\Omega b}. \tag{5}$$

The only other independent, adjustable dimensionless parameter is the magnetic Reynolds number, $Re_m\equiv UL/\eta$. We define Re_m using the sphere radius and impeller tip speed $Re_m\equiv\Omega ba/\eta$. The magnetic Reynolds number quantifies the ratio of field advection (twisting, stretching, etc.) to resistive diffusion. Thus, this number must be greater than unity to produce a dynamo. The (hydrodynamic) Reynolds number, $Re\equiv\Omega ba/\nu$, is related to the magnetic Reynolds number by the ratio of kinematic viscosity to magnetic diffusivity. This ratio, known as the magnetic Prandtl number $Pr_m\equiv\nu/\eta$, is a property of the fluid. For sodium at 120 °C, this number is small ($Pr_m=8.3\times10^{-6}$), meaning flows with $Re_m>1$ will be highly turbulent ($Re>10^5$).

4. Results

4.1. Time series

The induced field dynamics change markedly with the interaction parameter. The five time series, shown in Fig. 2, characterize the magnetic field fluctuations observed over the range of interaction parameter in our experiment. Except for Fig. 2b, the time series for the smooth wall case are qualitatively similar to those in the case with baffles. The interaction parameter ranges for the different regimes are shown in Table 3.

Fig. 2 shows magnetic field time series for increasing applied fields for $\Omega/2\pi=10$ Hz. For small fields (Fig. 2a) the induced field fluctuates erratically, similar to the fluid velocity fluctuations of the underlying turbulence; the magnetic field is simply a passive

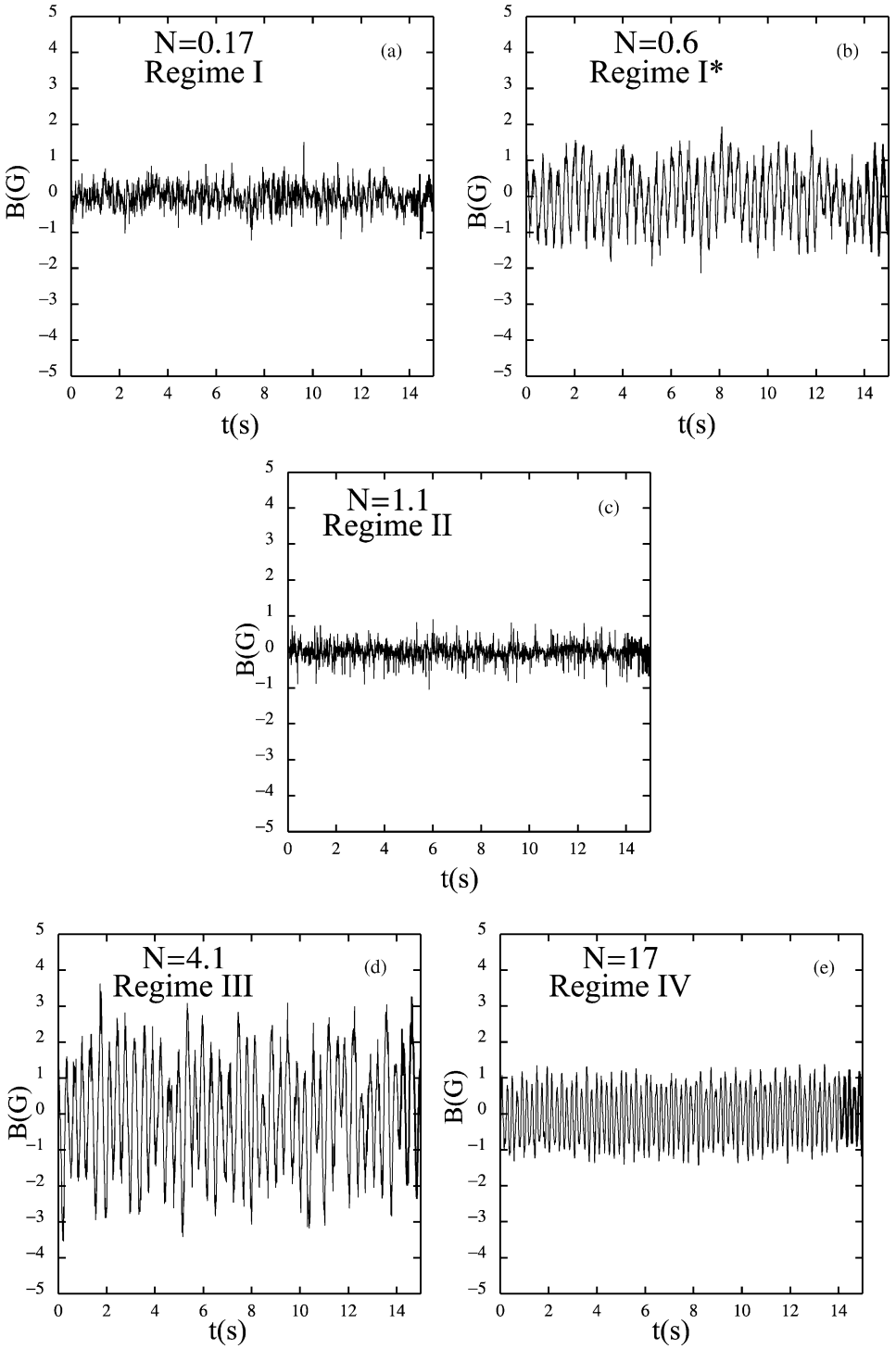
N=0.17
Regime I
(a)
N=0.6
Regime I*
(b)
N=1.1
Regime II
(c)
N=4.1
Regime III
(d)
N=17
Regime IV
(e)
B(G)
t(s)

Table 3
The five regimes

Regime	Range (smooth walls)	Range (baffles)	Beginning boundary	Character
I	$0 < N < 0.3$	$0 < N < 0.3$		$\vec{B}$ passive vector
I*	$0.3 < N < 0.6$		Increasing slope of σ (see Fig. 9a)	$m = 1$ oscillations
II	$0.6 < N < 2$	$0.3 < N < 3$	First peak of σ (see Fig. 9)	Turbulence suppression
III	$2 < N < 9$	$3 < N < 7$	Start of induced field frequency peak (see Fig. 3)	$m = 2$ oscillations, f depends on B_{ext}
IV	$N > 9$	$N > 7$	Start of frequency locking (see Fig. 3)	$m = 2$ oscillations, f independent of B_{ext}

vector. Increasing the applied field strength, large oscillations emerge in regime I* (Fig. 2b), though only with smooth walls. In regime II (Fig. 2c), the fluctuations become smaller despite a larger applied field, indicating the suppression of turbulence. This is consistent with other studies of MHD turbulence, where turbulence suppression by applied fields is well established (Cowling, 1957; Moreau, 1990). In the smooth wall case, regime II also shows a suppression of the regime I* oscillations. In regime III (Fig. 2d), another instability forms as large oscillations in the time series emerge. The frequency of these oscillations increases with the applied field (detailed in Section 4.2). Finally, in regime IV (Fig. 2e), the oscillations acquire modulations, and lock onto subharmonics of the impeller rotation rate.

4.2. Composite Fourier spectra

Now we examine the power spectra to show how the system evolves through the different regimes. Fig. 3 shows power spectra of magnetic field as a function of applied field for a fixed rotation rate. Each horizontal line of the images is formed from the power spectrum at one value of the applied field. In the figure we have indicated the regimes that are exemplified in Fig. 2. In regime I, the power spectra is broadband and increases in intensity as the applied field is increased. In regime I* (Fig. 3a only), we see the emergence of a frequency peak. In regime II, where turbulence is suppressed, the intensity decreases with increasing applied field. Regime III begins with the emergence of an intense single frequency peak whose frequency increases with applied field (nearly linearly for the case with baffles, Fig. 3b).

A standing Alfvèn wave resonance frequency would also increase linearly with applied field; however, there are at least four problems with an Alfvèn wave origin for these oscillations. First, the frequency range is too low. The Alfvén velocity, $v_A = B/\sqrt{\mu_0 \rho}$, at 1000 G for our experiment is 2.8 m/s. The resulting resonance for a box of length $2b$, the sphere diameter, is thus 9.9 Hz—several times too large for the observed oscillations at 1000 G for the Re_m explored in our experiment. Second, the induced field frequencies in regime III increase with rotation rate, as evidenced by the collapses in Fig. 4. No obvious fluid motion would modify an Alfvén wave resonance in this way. Third, the (extrapolated) zero field induced field frequency in our experiment is non-zero. Lastly, in Fig. 3a, the frequency increase in regime III deviates more significantly from a linear trend, and there is an even lower frequency peak ($\sim 0.1\ \Omega$) that changes slowly (and nonlinearly) with applied field.

Fig. 2. Time series of the induced magnetic field measured outside the sphere at the equator for each of the regimes (for smooth walls). In each, the time-averaged magnetic field has been subtracted. The magnetic Reynolds number is $Re_m = 7.5$, corresponding to an impeller rotation rate $\Omega/2\pi = 10$ Hz. The interaction parameter is shown for each time series. As the interaction parameter increases: (a) regime I, the induced magnetic field exhibits turbulent fluctuations, as the magnetic field acts as a passive vector; (b) regime I*, an instability with large oscillations at approximately 30% the impeller rotation rate occurs (with smooth walls only); (c) regime II, the turbulence and oscillations are suppressed by the Lorentz forces; (d) regime III, large coherent oscillations occur again where the frequency depends on the applied magnetic field; and (e) regime IV, the oscillations decrease in magnitude, acquire a modulation, and the frequency locks (for the case with baffles) to half the impeller rotation rate.

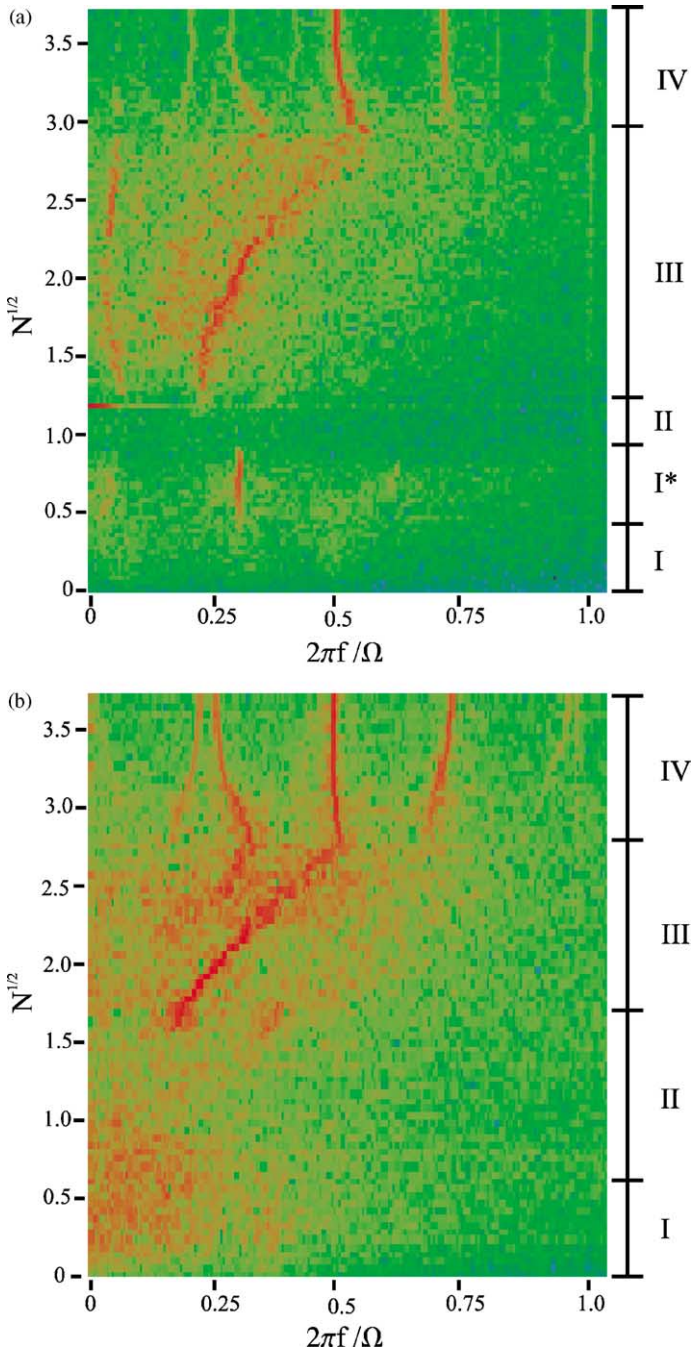

Fig. 3. Images composed of induced field power spectra. Applied field increases up the page, where each horizontal line is a power spectrum of the induced field for smooth walls (a) and with baffles (b). The applied field increases in steps of ≈22 G (a) and ≈18 G (b). The deviation from a linearly-increasing field in this figure is estimated to be less than 1% and the nonlinearities are limited to the highest field values due to coil heating. Color indicates logarithmic intensity, from highest to lowest: red–yellow–green–blue. The impeller rotation rate is 10 Hz ($Re_m = 7.5$). The regimes are indicated on the right. Both spectra were obtained from a probe at the equator, though the qualitative features are similar at any point outside the sphere.

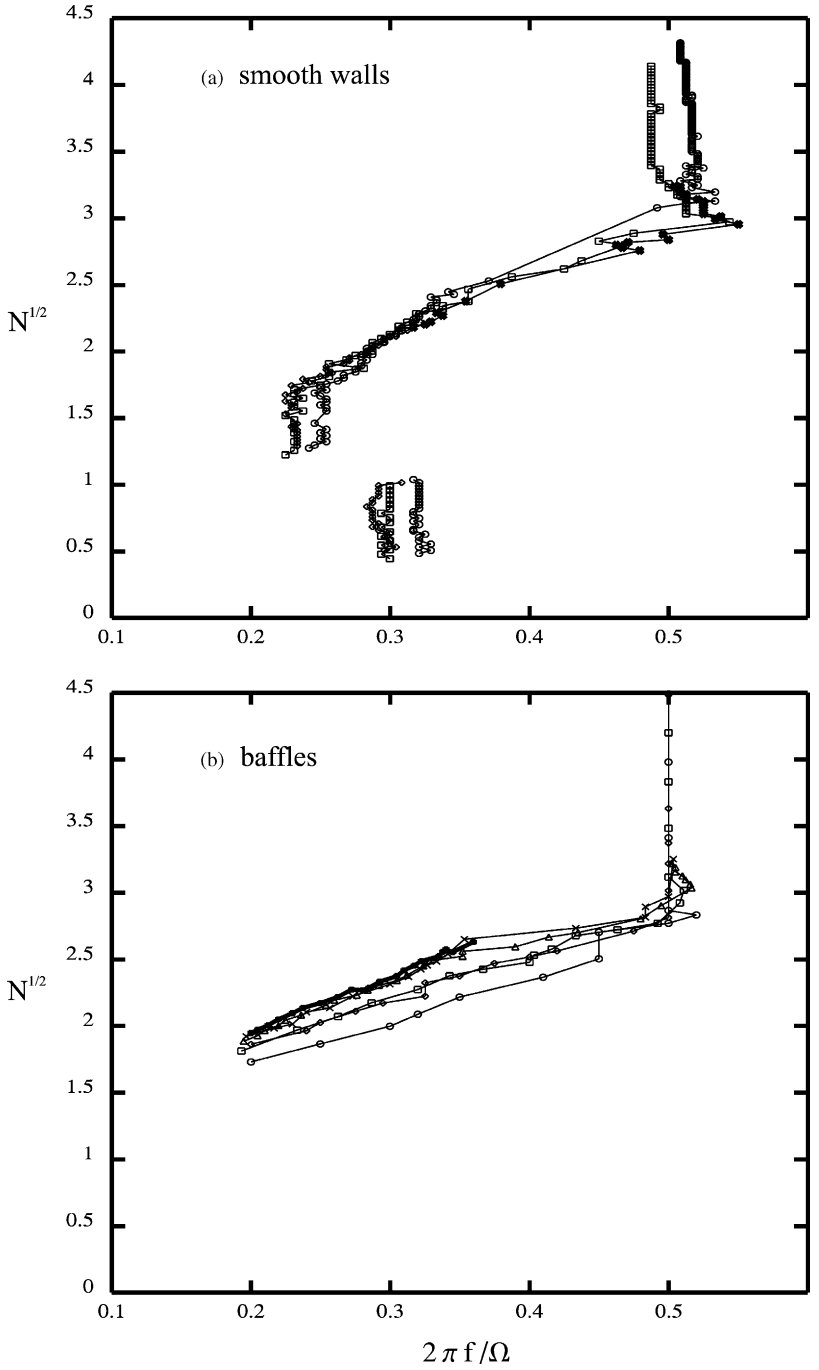

Fig. 4. The most intense induced field frequency in regimes I*, III and IV for impeller rotation rates: 5 Hz, $Re_m = 3.8$ (○); 7.5 Hz, $Re_m = 5.6$ (□); 10 Hz, $Re_m = 7.5$ (◇); 12.5 Hz, $Re_m = 9.4$ (△); 15 Hz, $Re_m = 11.3$ (×); and 22.5 Hz, $Re_m = 18.75$ (+). Data is shown in (a) with smooth walls and (b) with baffles. The frequency and applied field have been made dimensionless using the rotation rate and the interaction parameter. $N^{1/2}$ is used instead of N here (and elsewhere) because the former is linear in B. In regime III, we have followed the $0.2 < 2\pi f/\Omega < 0.5$ peak and not the peak $2\pi f/\Omega < 0.1$.

Regime IV begins where the single frequency of regime III reaches $2\pi f = \Omega/2$, at which point the single frequency splits into three frequencies and locks onto the rotation rate. The central peak at $2\pi f = \Omega/2$ is nearly independent of the applied field strength; two sideband modulations near $2\pi f = \Omega/4$ and $3\Omega/4$ change slowly with the applied field.

We have extracted the dominant frequency peak in regimes I*, III, and IV as it changes with applied field for multiple rotation rates, as shown in Fig. 4. The frequency and magnetic field strength were made dimensionless using the rotation rate and the interaction parameter. Were the interaction parameter the only relevant parameter, the curves would collapse. However, the collapse is imperfect, especially in regime III—a given oscillation frequency occurs at a somewhat higher interaction parameter for higher impeller rotation rates. Also, there are secondary features—an overshooting of the $2\pi f = \Omega/2$ frequency, as well as the frequency remaining unchanged for small ranges of interaction parameter—that depend on magnetic Reynolds number. These are likely Re_m effects, because the magnetic Reynolds number is the only other relevant, independent non-dimensional parameter.

4.3. Induced field structure

The induced field oscillations in regimes I*, III, and IV are present at every point near the sphere's surface. To examine the spatial structure of these oscillations, we calculate correlations in azimuthal and poloidal Hall probe arrays.

Fig. 5 shows the spatial correlations, along with schematic versions of the induced field derived from these correlations, for regimes I* and IV. Regime III (not represented in this figure), like regime IV, has an $m = 2$ correlation at the equator and is equatorially anti-symmetric, but it does not have a well-defined poloidal wave number l, as correlations near the poles are weak (see Fig. 8d). Also, in regime IV there is an $m = 0$ component mixed in with the $m = 2$ correlation near the pole (Fig. 5e). In Fig. 6, cross-correlations between judiciously chosen probes as a function of interaction parameter show how the modes, described above, evolve with interaction parameter.

From temporal cross-correlations on the equatorial array, we can determine if the induced field patterns precess, and if so in which direction. We first compute the cross-correlation function for pairs of probes:

$$C(\tau, \phi) = \frac{\langle A(t)B(t+\tau)\rangle}{\sqrt{\langle A(t)^2\rangle\langle B(t+\tau)^2\rangle}}.$$

Here, $A(t)$ and $B(t)$ are magnetic field time series with time averages subtracted, from Hall probes separated azimuthally by an angle ϕ; brackets indicate time averages. The time lag that maximizes the correlation, τ_{max}, determines the time for the pattern to travel the angular distance ϕ. We find that τ_{max} increases linearly with angular separation, indicating azimuthally-traveling waves or precessing vortices in the fluid motion. From the relative signs of τ_{max}, ϕ, and the impeller rotation direction, we found that this motion was prograde (i.e. in the direction of impeller rotation).

Fig. 7 shows the precession speed deduced with this technique as a function of interaction parameter. Shown also is the peak induced-field-spectral-frequency scaled by m, for the same Re_m. The two curves collapse for most values of interaction parameter, suggesting that the induced field oscillations are the result of precessing spatial patterns. This collapse provides new insight into the dynamics of regime

Fig. 5. Correlations of induced field. The cross-correlation as a function of poloidal angle for regime I* (a) and regime IV (b), and as a function of azimuthal angle at the equator for regime I* (c) and regime IV (d), and as a function of azimuthal angle near one pole in regime IV (e). The cross-correlation is defined as: $C(x) = \langle A(t)B(t)\rangle/\sqrt{\langle A(t)^2\rangle\langle B(t)^2\rangle}$ where $A(t)$ and $B(t)$ are magnetic field time series with time averages subtracted, from Hall probes separated by an angle x; brackets indicate time averages. In each array, cross-correlations were computed relative to one probe, giving correlation as a function of angular separation. In the poloidal array, the probe nearest one pole was chosen as a reference, since that permitted the largest angular separation. In the array encircling a pole, the reference probe was chosen arbitrarily (the results are independent of reference). These measurements were taken at $Re_m = 7.5$ ($\Omega/2\pi = 10$ Hz) with smooth walls. In (c), the probe at 103° is offset from the equator, which explains the deviation from the $m = 1$ trend. In the lower left corner, a schematic shows the idealized induced field pattern consistent with correlation data for regimes I* and IV. The field component is in the cylindrical-radial direction. White and black indicate positive and negative induced field. The patterns precess in the prograde direction.

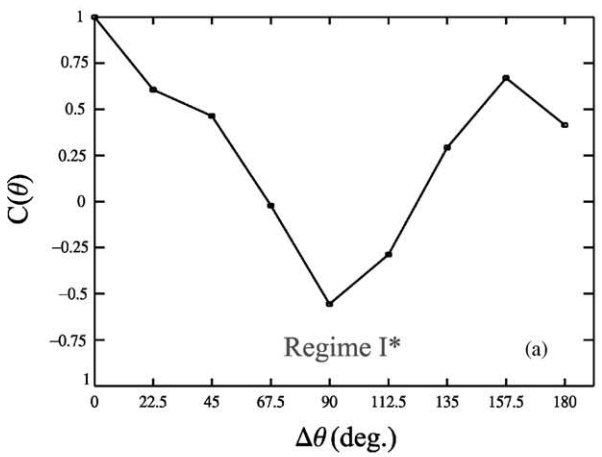

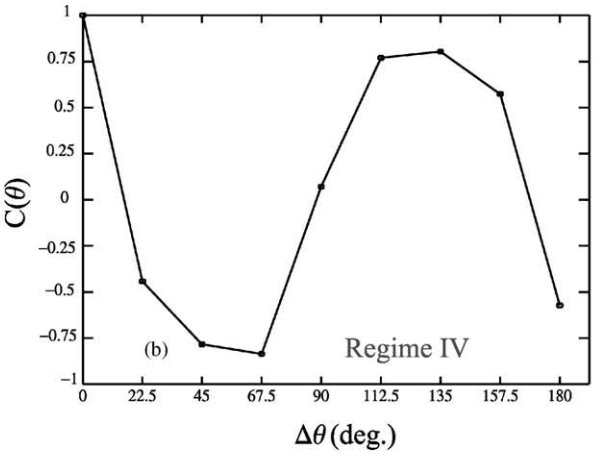

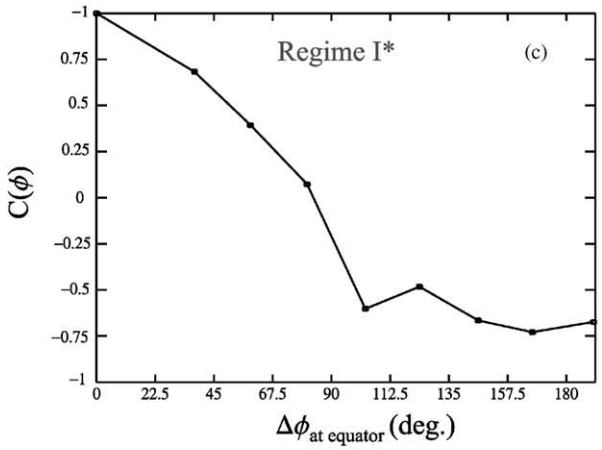

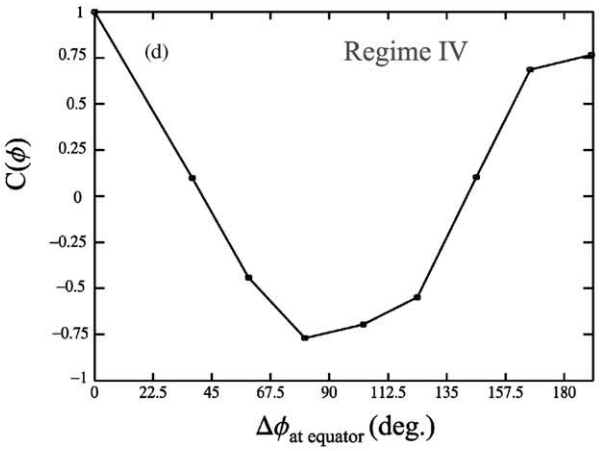

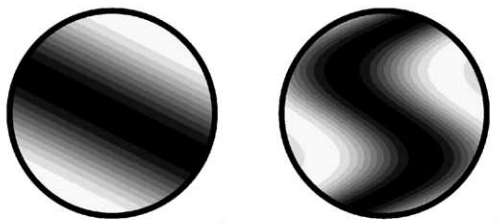

Regime I*

smooth walls only
m=1
l=2

Regime IV

smooth & baffles
m=2
l=3

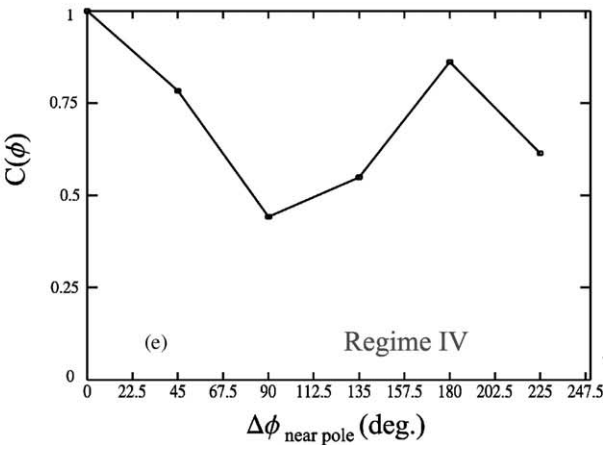

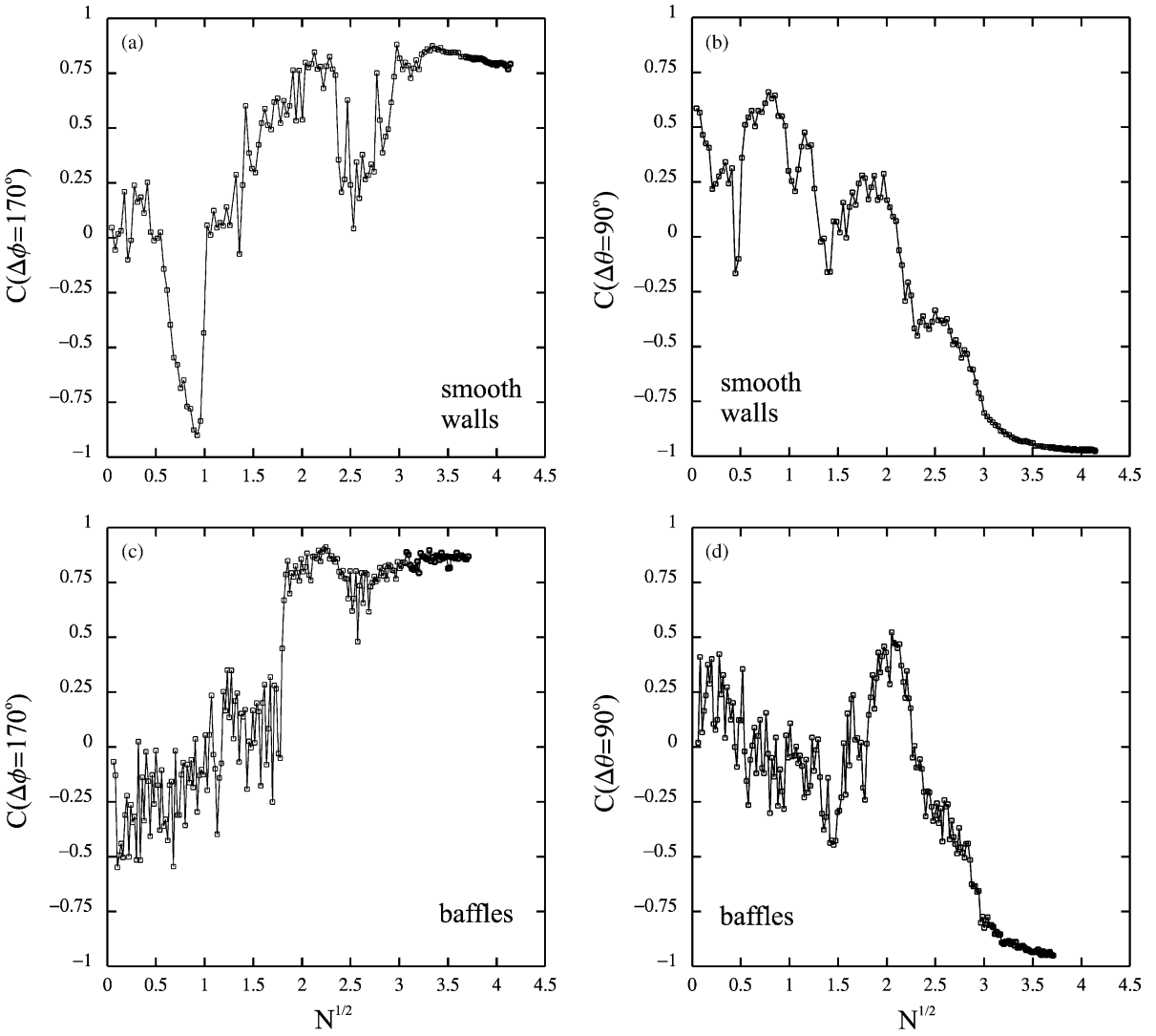

Fig. 6. Correlations vs. interaction parameter. The left two panels show cross-correlation between two probes separated by 170° on the equatorial array with smooth walls (a) and with baffles (b). The right two panels show cross-correlations between two probes, each 45° from the equator on opposite sides with smooth walls (c) and with baffles (d). The cross-correlations in (c) and (d) were computed from 4 s time series and in (a) and (b) from 16 s time series. This measurement time difference is reflected in Fig. 6c and d where the correlation has more scatter at low interaction parameter.

III: the frequency peak increasing with applied field is caused by an increasing precession velocity of an $m = 2$ pattern in the flow. However, for $N^{1/2} > 3.0$, the deduced precession velocity is somewhat greater than the peak frequency scaled by m. This discrepancy is likely associated with the observed modulations in regime IV (see Figs. 2e and 3).

Since coherent structures (with relatively long correlation times) are precessing azimuthally, the pole-to-pole array should provide a nearly complete picture of the induced field dynamics. Fig. 8 shows induced field space–time diagrams for this array. Six diagrams are shown—one each for regimes I, I*, II, and IV, and two for regime III. In regime I*, we see

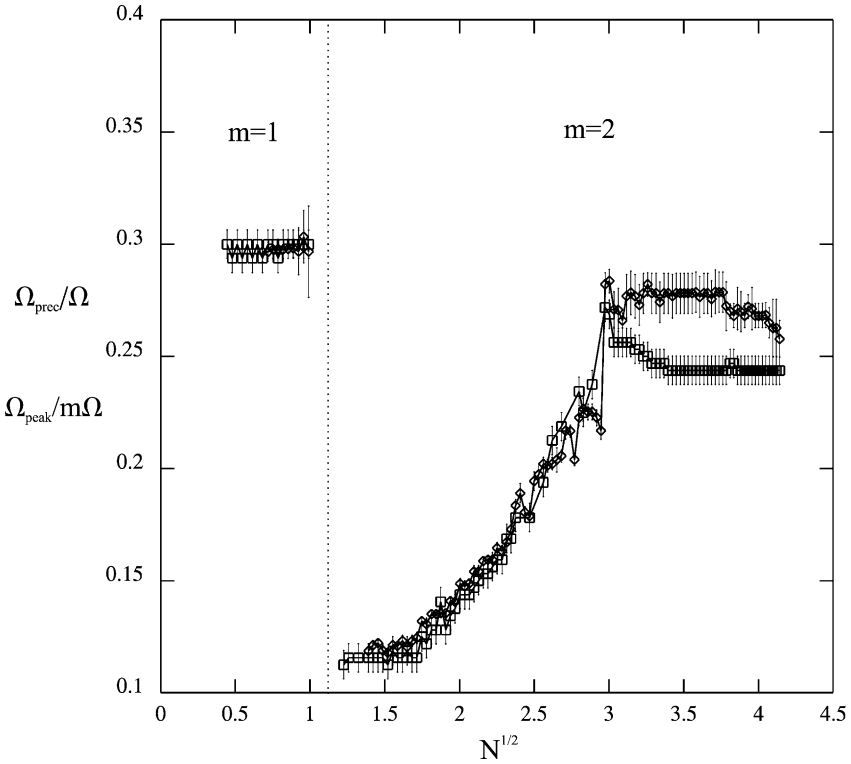

Fig. 7. Dimensionless precession frequency from cross-correlations (◇), and frequency peak from induced field power spectra scaled by m (□), vs. interaction parameter. The precession frequency was obtained by first maximizing the cross-correlation function $C(\tau, \phi)$ for probes separated by ϕ on the equatorial array. The precession angular velocity is a linear fit to angular separation ϕ vs. optimum time lag, $\tau_{max}(\phi)$. The error bars for precession speed indicate the standard deviation of the fit. The error bars on the induced field frequency peak is the bin size in the Fourier transform algorithm. Both frequencies have been scaled by the rotation rate $\Omega/2\pi$. These measurements were taken at $Re_m = 7.5$ ($\Omega/2\pi = 10$ Hz) with smooth walls.

the oscillations appear to be caused by precessing (perhaps columnar) structures tilted relative to the axis of rotation (Fig. 8b). Precessing structures also appear to cause the oscillations in regime III (Fig. 8d and e). As one looks from pole to pole in that regime, it appears the structures are divided into zones. The dynamics between the zones is not strongly correlated, reflecting the lack of a distinct poloidal wave number in regime III. Two things happen in Fig. 8d and e as the interaction parameter increases: the coherence between the zones increases, and the zonal boundary shifts toward the equator. Both effects are also evident in Fig. 6b and d, where the anti-correlation increases steadily past $N^{1/2} = 2$.

In regime IV, the coherence between zones increases further still. Here, the structures seem more wavy than divided discretely into zones. Additional boundaries have formed in between the first and second probes and also between the last two probes directly opposite the equator (not shown, see Fig. 8 caption). These wavy structures give rise to the $l = 3$ correlation shown in Fig. 5b.

It should be noted that in Fig. 8b, d–f the strongest oscillations (i.e. where the peaks are brightest and most sharply defined) occur at large angles. This asymmetry most likely results from asymmetry in the impellers: the impellers have the same helicity so that faced opposite and co-rotating—as in our experiment—one impeller “scoops” while the other does not (see Fig. 1b). The scooping impeller is at large θ in Fig. 8; thus, the greater entertainment of the scooping impeller apparently enhances the instability.

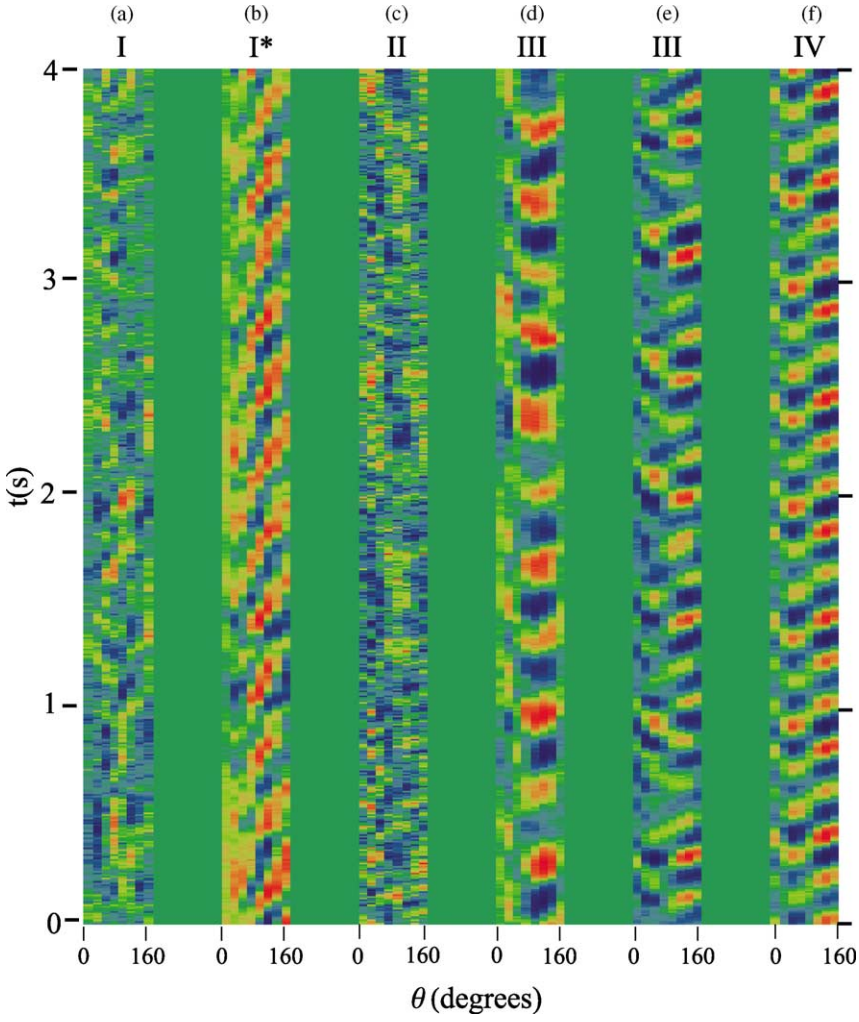

Fig. 8. Six different space–time diagrams of induced field in the poloidal array. Each horizontal line shows the magnetic field intensity (indicated by color) vs. poloidal angle; time increases up the page. The time averages of each probe have been subtracted. Red indicates the highest field values and blue the lowest. Six diagrams, (a)–(f), are shown with the regime indicated above each. The corresponding interaction parameters are: (a) $N^{1/2} = 0.28$, (b) $N^{1/2} = 0.75$, (c) $N^{1/2} = 1.1$, (d) $N^{1/2} = 2.1$, (e) $N^{1/2} = 3.0$, and (f) $N^{1/2} = 4.0$. All diagrams are for the smooth wall case and $Re_m = 7.5$ ($\Omega/2\pi = 10$ Hz). In each diagram, eight probes are used. Note that each diagram is not centered about the equator—the probe nearest the right pole failed during the run and was not included.

4.4. Induced field fluctuation magnitudes

Another way to observe interaction parameter effects is through the magnitudes of the induced field fluctuations. Fig. 9 shows the standard deviation of the induced field σ as it changes with the external field for a single rotation rate. In regime I, the magnetic field is a passive vector in the turbulent flow, and the standard deviation increases linearly with applied field. In regime I* (Fig. 9a only), as the $m = 1$ instability forms, the fluctuations increase more sharply (though still linearly) with applied field. Then, in regime II, the fluctuations diminish with increasing applied field—a sign that turbulence in the velocity field is suppressed. The fluctuations increase again in regime III due to the $m = 2$ instability. This rise in

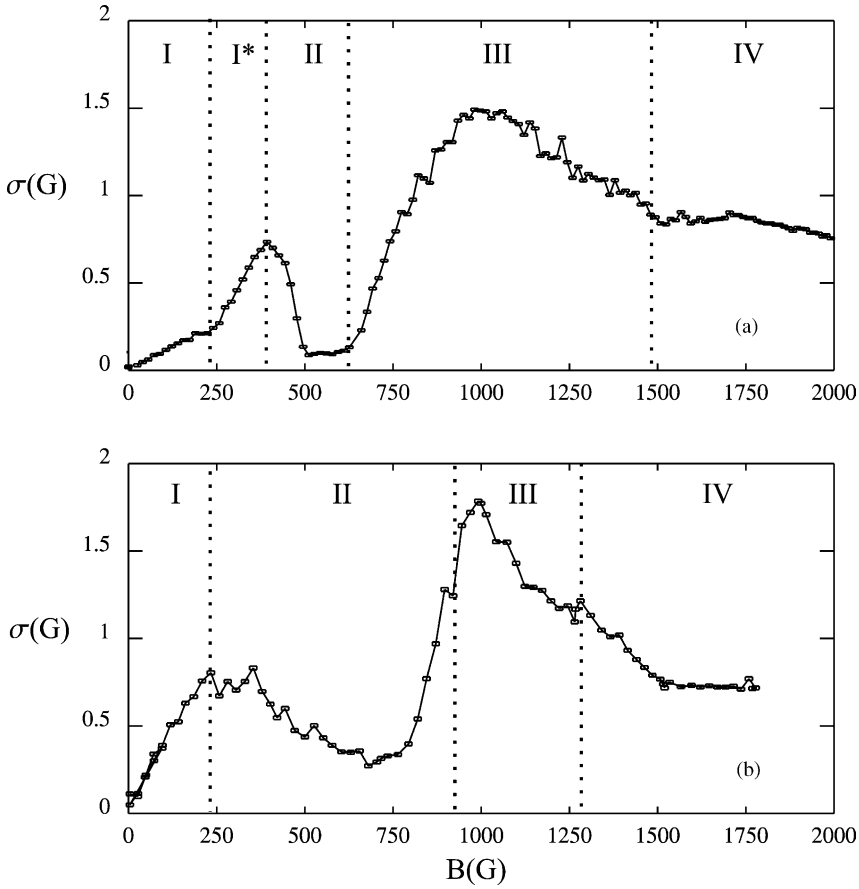

Fig. 9. Standard deviation of the induced field vs. applied field (a) with smooth walls and (b) with baffles. Both (a) and (b) are for $Re_m = 7.5$. The field fluctuations were measured in the radial direction at the equator. The regimes are indicated.

σ occurs despite a further suppression of turbulence in regime III, evident from the decrease of broadband content in the power spectra. The oscillation magnitude then decreases in the latter half of regime III. Finally, in regime IV the oscillations decrease further and then change only slowly with the applied field.

The fall of the standard deviation in regimes III and IV is due partly to the shifting zones seen in Fig. 8. Indeed, the standard deviation curves for probes at different polar angles look somewhat different. For instance, the peak in regime III occurs at different interaction parameter, and for some probes the standard deviation increases with applied field in regime IV. This difference can be seen qualitatively in Fig. 8, as described above in Section 4.3. The fall of the standard deviation in regime II, however, seems to be a general suppression of turbulence.

Fig. 10 shows the induced field standard deviation for several magnetic Reynolds numbers. A collapse is attempted for these data by scaling the applied field using the interaction parameter, and by scaling the magnitudes by a characteristic field value, $B_c \equiv \sqrt{\rho\mu_0 ab^3\Omega^3/\eta}$.

This characteristic field value is arrived at from the equations of motion. Assuming large Reynolds number and moderate interaction parameter, the advective force and the Lorentz force are both dominant and comparable in magnitude. Thus, we obtain from the

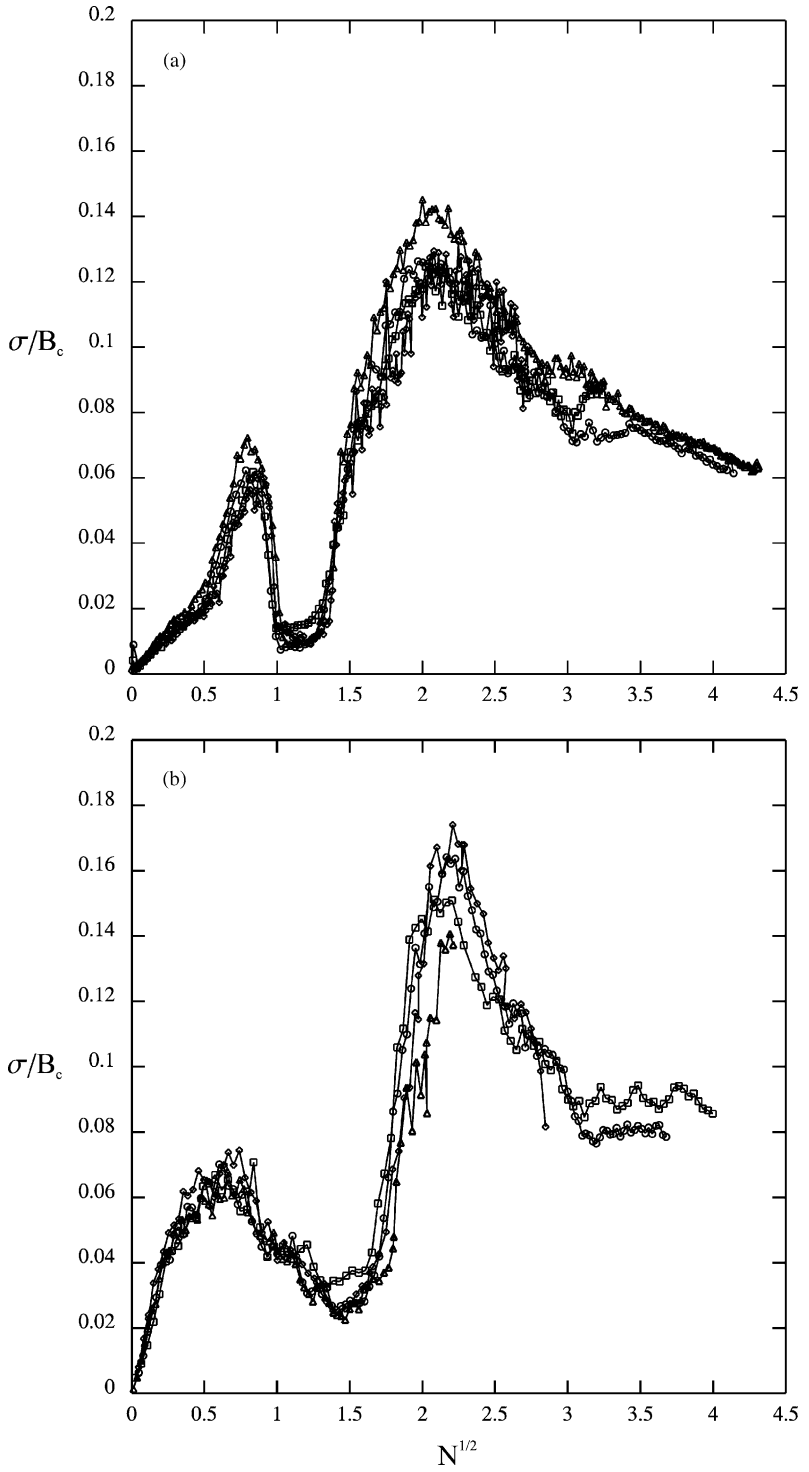

Fig. 10. Dimensionless standard deviation of the induced field as a function of the applied field (a) with smooth walls and (b) with baffles for the magnetic Reynolds numbers: 3.8 (○), 7.5 (□), 15 (△), and 18.75 (◇). The data are made dimensionless using the interaction parameter and a characteristic magnetic field, $B_c \equiv \sqrt{\rho\mu_0 ab^3\Omega^3/\eta}$.

dimensional form of Eq. (1),

$$(\vec{u}\cdot\vec{\nabla})\vec{u} \sim \frac{1}{\rho\mu_0}(\vec{\nabla}\times\vec{B}_{\mathrm{ind}})\times\vec{B}_{\mathrm{ext}}$$

which implies

$$\rho\mu_0 U^2 \sim B_{\mathrm{ext}} B_{\mathrm{ind}}. \quad (6)$$

From the induction equation (where the time derivative term has been dropped, since it should be somewhat smaller than the diffusive term):

$$\vec{\nabla}\times\vec{u}\times\vec{B}_{\mathrm{ext}} \sim \eta\nabla^2\vec{B}_{\mathrm{ind}}.$$

This implies that

$$B_{\mathrm{ind}} \sim B_{\mathrm{ext}} UL/\eta. \quad (7)$$

The proportionality in Eq. (7) should not be taken as an equality due to ambiguities in the choice of velocity and length scales from the induction equation.

Eliminating B_{ext} from (6) and (7) yields

$$B_{\mathrm{ind}} \sim B_{\mathrm{c}} \equiv \sqrt{\rho\mu_0 ab^3\Omega^3/\eta}$$

where the impeller tip speed Ωb has been substituted for U and the sphere radius a for L. Thus, we might expect the standard deviation of the induced field to scale as B_{c}. From Fig. 10, we see that making the standard deviation of B_{ind} dimensionless as σ/B_{c} and B_{ext} dimensionless as $N^{1/2}$ causes the different Re_{m} cases to collapse.

Taken together, Figs. 4 and 10 demonstrate that the interaction parameter controls much of the qualitative changes in the system for the full range of Re_{m} values and applied fields explored in this experiment.

4.5. Motor torque

We also observe significant changes in the torque as the interaction parameter is increased. Fig. 11 shows

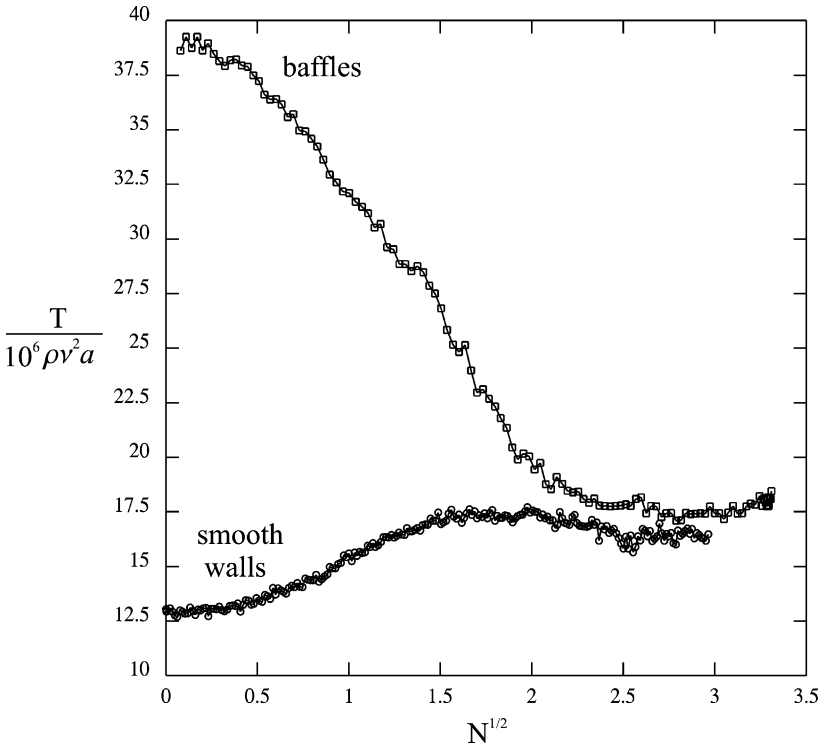

Fig. 11. Dimensionless torque as a function of interaction parameter for a rotation rate of 15 Hz ($Re_{\mathrm{m}} = 11.3$), with smooth walls (○) and with baffles (□). The torque shown is the average of both motors. Because the data sets were (necessarily) taken during different runs, there is an uncertainty in the relative offset of the two curves due to unknown differences in frictional losses in the seals. This offset is estimated to be less than 5% of the smooth wall zero field value.

the motor torque required to co-rotate the impellers at a fixed rotation rate ($Re_m = 11.25$) versus $N^{1/2}$. The top curve is with baffles and the bottom with smooth walls. The salient and somewhat surprising feature of this figure is that with increasing magnetic field the torque *increases* with smooth walls and *decreases* with baffles.

Two other differences in the two torque curves are apparent as well. First, at zero field the torque is lower with the smooth wall case. This is not surprising. The torque required to spin the impellers is a measure of the momentum transfer from the impellers to the spherical container. The baffles, which entrain fluid in the azimuthal direction—the dominant component of the mean flow—will thus aid this momentum transfer. Finally, the two curves converge (to within uncertainty) at high interaction parameter. This convergence, occurring also for other rotation rates, appears robust.

5. Discussion

In this section, we will interpret our measurements, and discuss their connection with prior scientific work and their relation to the Earth and the Sun.

Applied magnetic fields are known to increase the rigidity of conducting fluids in the direction of the field. As the applied field increases in our experiments, a cylinder of sodium between the impellers would become increasingly coupled to the impeller rotation rate. Correspondingly, the fluid outside the cylinder would be increasingly tied to the boundary. As this happens, we might expect momentum transport from the impellers to the wall to decrease, reducing drag and thus torque. Indeed, with baffles the required torque decreases with imposed field over a large range of N.

For small applied fields the drag is greater with rough walls than with smooth. One might thus expect the torque decrease to be weaker without baffles. However, with smooth walls the torque *increases* with applied field. A possible mechanism for this increase involves how the applied field affects the boundary layers. As the applied field increases, the Hartmann layer at the sphere wall becomes thinner, increasing the viscous drag across it. This would increase the coupling between the fluid and the outer wall, causing the torque to increase with applied field. The case with baffles does not show the effect of the thinning boundary layers however (i.e. the torque does not increase with applied field). This discrepancy is likely due to the way angular momentum is transferred to the wall in the two cases. With smooth walls, viscous boundary layers alone control the momentum transport. In the other case, pressure drops across the baffles apparently cause most of the transport.

The torque with smooth walls plateaus and then decreases slightly around $N^{1/2} = 1.5$. A similar plateau occurs with baffles around $N^{1/2} = 2.5$ (Fig. 11). There is no obvious connection between this apparent saturation and changes in the induced field character. The best connection, which is rather tenuous, is found in Fig. 6b and d: the trend toward equatorial anti-symmetry begins roughly at the same interaction parameter where the torque deviates from its linear trend in Fig. 11. The torque curves may be best explained by changes in the velocity field that are not reflected in the magnetic field data. In the future, we plan to measure the velocity directly using ultrasound velocimetry.

The picture involving the tendency for magnetic fields to tie fluid along field lines also leads to an explanation for the observed oscillations in regimes I*, III, and IV. In the large field limit, the fluid forms a cylinder between the impellers undergoing solid body rotation while the surrounding fluid is stationary. As a rotating cylinder of sodium forms, so would a strongly sheared boundary. Traveling waves or precessing vortices would likely form at this boundary, giving rise to the observed oscillations in the induced field.

Experiments by Lehnert (1955) first showed, in a very different geometry, how magnetic rigidity can lead to vortex formation in liquid metals. In the absence of applied fields Lehnert's experiment was laminar, whereas ours is highly turbulent. Experiments similar to Lehnert's have been performed by Moreau (1990), Brito et al. (1995).

In a system similar to ours, Hollerbach and Skinner (2001) find (numerically) vortices forming in a magnetically-induced shear layer. Like ours, their flow was in a spherical container with strong magnetic fields imposed parallel to the axis of rotation; however, their driving was a rotating inner sphere, not co-rotating impellers. At high fields they find a solidly-rotating cylinder tangent to the inner sphere; thus, we would expect the two systems' dynamics to converge at large N. They found vortices precessing

at a fraction of the inner sphere rotation rate in their system. The number of vortices depended mainly on the applied field and the boundary conditions (conducting or non-conducting), though Reynolds number effects were also observed.

Though we are unable to measure the sodium velocity in our experiment directly, our magnetic field measurements are consistent with the precessing vortex patterns described by Hollerbach and Skinner. In particular, we infer velocity patterns in our experiment similar to the $m = 1$ and 2 instabilities described by Hollerbach and Skinner. However, extrapolating from Hollerbach and Skinner's study to our parameter range we would expect much higher m modes to be most unstable. For example, in our experiments for a magnetic field of 1000 G (expressed in their paper using the Hartmann number, the ratio of the magnetic to viscous time scales), Hollerbach and Skinner predict $m = 5$ ($m = 12$) for insulating (conducting) boundary conditions to be the first unstable mode.

The critical Reynolds numbers for both boundary conditions are $Re \approx 1000$, which are much lower than the lowest obtainable Reynolds number in our experiment (extremely low rotation rates are difficult to control accurately). However, for two values of applied field (for each boundary condition) they increased the Reynolds number past the critical values to observe how the system equilibrates in the supercritical regime. They found that the torque needed to spin the inner sphere increased at the onset of the first instability. In our runs without baffles we also observe the torque increasing at the instability onset. In our experiments we increase the magnetic field to induce the instability, since we can not lower the rotation rate below the critical Reynolds number for even the highest field obtainable. Notice in Fig. 11, in the smooth wall case, the torque is nearly constant until $N^{1/2} = 0.4$; in Fig. 4a, the $m = 1$ instability also occurs at $N^{1/2} = 0.4$. The torque for that case then steadily increases and then decreases with applied field, seemingly independent of further instabilities.

As the Reynolds number is increased past its critical value, Hollerbach and Skinner observe that the azimuthal wave number m is reduced, through a subcritical bifurcation. For the range of Reynolds number that they study (up to approximately twice the critical value) the m value is reduced at most by one. The Reynolds number in our experiment, by contrast, is hundreds of times their critical value. That we only observe low m instabilities in our experiments (instead of the higher m instabilities that Hollerbach and Skinner predict to be most unstable) is evidence for additional m reductions occurring at higher supercriticality. It is not clear why $m = 2$ is favored at high applied field in our experiment, nor why $m = 1$ is favored at intermediate applied field. In fact, Hollerbach and Skinner never find an $m = 1$ instability. It is possible that $m = 1$ modes are only seen at high Reynolds number or are a feature associated with geometric differences. In our experiment, the progression from $m = 1$ to 2 as the applied field increases is similar to the favoring of higher m modes as the applied field increases that Hollerbach and Skinner observe. It appears that at high supercriticality some features of the regime near criticality remain (e.g. preferring high m modes at high applied fields) while other features change (e.g. the appearance and then suppression of a previously unseen $m = 1$ mode).

Another feature that is due to either high supercriticality or geometric differences is the equatorial symmetry of the instabilities. Hollerbach and Skinner find only equatorially symmetric instabilities. Our experiments show both symmetric and anti-symmetric instabilities. More specifically, the $m = 1$ instability corresponds to an $l = 2$ (i.e. equatorially symmetric) pole-to-pole induced field correlation (Fig. 5a), and the $m = 2$ to an $l = 3$ (anti-symmetric) correlation (Fig. 7b). Note that these correlations are not the simplest symmetric and anti-symmetric states possible. As seen in Fig. 8 and as discussed above, the transition to equatorial anti-symmetry is due to apparent undulations in columnar vortices.

Interestingly, Moreau (1990) speculates that such undulating columnar vortices parallel with the applied field would form for $N \gg 1$. This prediction came from a theoretical extension to much larger applied fields for the experiment described in Alemany et al. (1979). The flow there was generated in a circular column of mercury by driving a grid at constant velocity. They only reached $N \approx 1$ and did not observe these vortices. For the large N limit Moreau concluded that the columnar vortices would undulate in the direction of the applied field with the characteristic length $l_\parallel \approx l_\perp N^{1/2}$, where $l_\perp$ is a characteristic length transverse to the applied field. This contrasts with our finding that as the interaction parameter is increased, $l_\parallel$ de-

creases (as new zones are added) (Fig. 8). There is little change in $l_\perp$ as that is slaved to the azimuthal wave number m. Indeed, in regimes III and IV, where $l_\parallel$ is decreasing, the wave number ($m = 2$) remains constant. The resolution of our pole-to-pole array is too low to more precisely determine how $l_\parallel$ scales with N.

Although we have not directly measured the velocity field, it seems most likely that the oscillatory instabilities result from precessing, wavy, columnar vortices in the flow aligned with the applied field. It is not clear, however, why the precession rate changes as it does with applied field (Fig. 7). Hollerbach and Skinner report precession rates for different applied fields and Reynolds number, but for a given Reynolds number they never report the precession rate for more than one applied field value. Hollerbach and Skinner also find that, for a given applied field, higher azimuthal wave numbers precess faster. For example, for a field equivalent to 350 G and a Reynolds number of $Re = 2000$ they find that the $m = 3$ solution precesses at 0.179Ω and the $m = 2$ solution at 0.15Ω. In contrast, we find in our parameter range that lower m modes precess faster (see Fig. 7). The magnitude of Hollerbach and Skinner's precession rates is comparable to ours.

Labbé et al. (1996) observe a similar phenomenon in a different system that may provide a clue to this changing precession speed mechanism. They experimentally studied co-axial, co-rotating von Kárman flow in air and found precessing vortices near the edge of their impellers. The precession period was found to increase with separation distance of their rotating disks. In other words, decreasing the length scale (set by the impeller separation) increases the vortex precession rate. In regimes III and IV, we found a shortening length for the poloidal zones with increasing interaction parameter. So it is possible this length-scale shortening leads to the increased precession rate. It would be interesting to vary the impeller separation in our experiment and repeat the measurements.

There is, however, a significant discrepancy in the dynamics of our system and Labbé et al.'s. In their experiment, the vortex precession is retrograde; in our experiment the precession, as measured at the equator (Section 4.3) and the array encircling one pole, is prograde. Their study, conducted using air, was of course non-magnetic, further suggesting that magnetic fields play a crucial, non-trivial role in the dynamics of our system.

5.1. Effect of the baffles

With or without baffles the overall dynamics in the system are quite similar. Note, for example, the similarity in the two cases in Figs. 3, 6, 9 and 10. However, there are four main effects produced by the baffles. Most significant is how the torque changes with applied field for a fixed rotation rate. With baffles the torque decreases with increasing applied field, and without baffles the torque increases. The magnitude of the torque decrease with baffles is larger than the increase without. Second, the baffles suppress the $m = 1$ oscillations that emerge in the intermediate range of interaction parameter. It appears this state is sensitive to the boundaries. This $m = 1$ instability begins at the same applied field as the turbulence-suppressing regime II with baffles (see Fig. 9). Third, the range of N values for regime III is increased, beginning at smaller N and ending at larger N (see Table 3). The dynamics in regime III, as described in Section 4.3, are postulated to result from precessing columnar vortices. Thus the baffles apparently suppress the formation (or precession) of the vortices, and better lock the vortex precession rate to half the impeller rotation rate. The latter effect is evident in Fig. 4, where the induced field frequency peak is one half for large interaction parameter with baffles but only approaches one half without.

Finally, the baffles increase the magnitude of induced field oscillations in regime I. As seen in Figs. 9 and 10, the slope of σ versus B_{ext} is steeper with baffles. The baffles either make a more turbulent flow (assuming $B_{\text{rms}} \sim u_{\text{rms}}$), or makes the flow more efficiently generate induced fields (i.e. Re_{m} is effectively made larger for a given rotation rate). This effect of the baffles disappears at higher interaction parameter.

5.2. Application to the Earth and Sun

Core–mantle coupling—exchange of angular momentum between the core and the mantle—is thought is to be responsible for variations in the Length of Day, and in the orientation of Earth's axis of rotation. The degree of coupling is also an important parameter in

many dynamo models (Roberts, 1988). Coupling can occur in a number of ways, including topographically or electromagnetically. These two processes are often considered separately (e.g. Jault et al., 1996; Aldridge et al., 1990). However, our results show that Lorentz forces and topography need to be considered together, at least in our parameter range. Indeed, the magnetic field can either enhance or weaken angular momentum transfer (≈50% over the range of interaction parameter in our experiment) to the outer case depending on the topography of the vessel walls (see Fig. 11). In our experiment the angular momentum transfer, with baffles and without, seems to converge at higher interaction parameter. This suggests that magnetic effects come to dominate and "wash out" pure topographic coupling when the interaction parameter is greater than about $N = 5$. The estimated values of interaction parameter in the Earth are much larger than in our experiment; thus, the Earth operates either in regime IV or in some higher regime of Lorentz force domination.

Maps of the radial component of the magnetic field for 1715–1980 at the surface of the Earth indicate structure having similarities to our data. In that interval, the radial component of the Earth's field shows a fixed pattern of four flux concentrations (lobes) placed anti-symmetrically about the equator (Gubbins and Bloxham, 1987). Similar to regimes III and IV in our experiment, these lobes are placed anti-symmetrically about the equator. Paleomagnetic evidence, which samples the Earth's field on longer time intervals, suggests that these lobes do drift, though more slowly than the characteristic westward drift velocity (Constable et al., 2000). In our experiment, magnetic structures also drift slowly compared to the characteristic velocity (i.e. the impeller rotation rate). The relatively slowly moving flux pattern in the Earth is commonly thought to be an effect of heat flux inhomogeneities at the core–mantle boundary (Bloxham and Gubbins, 1987). However, our experiment, having no such inhomogeneities, suggests this motion could be a more robust dynamical feature. Indeed, one might guess that global rotation or the different forcing of the flow in the Earth would frustrate the instabilities seen in our experiment. Future experiments will determine how robust these instabilities are.

There is a length scale for which the flow within the core has the same interaction parameter as our experiments. This is approximately 10^{-5} the radius of the core, or about 30 m. One obvious location where the dynamics at this scale could affect geomagnetic observables are the core–mantle and inner core boundary layers. The boundary layers (thermal and Ekman) act as valves for both heat and momentum flux through the outer core. Our observations of the effects of Lorentz forces and roughness (baffles) on momentum transport may apply to these boundary layers. In addition to the effects on angular momentum transport discussed above, there should be Lorentz force effects on heat flux and core cooling. It has been argued that the turbulent momentum and heat flux are slaved together (by use of the Reynolds analogy, i.e. a unity turbulent Prandtl number) (Kays and Crawford, 1980). Using this concept and our observations of torque dependence one might expect that the heat flux from the rough core–mantle boundary is reduced when the dynamo first turns on. This might act as one saturation mechanism for the geodynamo. Future experiments are needed to directly probe the effects of Lorentz force on heat flux.

On this note, we recognize that our experiment is not an ideal geophysical model. One obvious shortcoming, as previously mentioned, is that our sphere is non-rotating—the fluid only rotates due to the co-rotating impellers. We are thus not in a low Rossby number regime as the Earth and most astrophysical objects are. Furthermore, a system driven by impellers is simpler than a system driven by convection, such as the Earth. The experimental compromises in this experiment were necessary, however, due to the difficulty and safety concerns in performing these types of experiments. Rotating our sphere would cause safety problems associated with decoupling the system from an overflow reservoir. Also, without impellers we would be unable to reach the magnetic Reynolds numbers reached in this experiment (without a *much* larger device), as convection causes weaker fluid velocities. Experiments with a new 60 cm diameter rotating convection apparatus are underway that may illuminate the effects of these simplifications.

The parameter ranges for the Sun come closer to overlapping with our experiment, though there are significant differences (e.g. the sun is plasma, and has a stratified structure). Unfortunately, uncertainties in diffusivity, field strength, and the relevant length scale yield a large range for estimates of the interaction

parameter for the Sun $1 < N < 10^4$ (Fisher et al., 2000; Gough and McIntyre, 1998; Charbonneau and MacGregor, 1997; Moffatt, 1978; Christensen-Dalsgaard et al., 1996; Gilman, 2000). The Rossby number of the Sun is $Ro \sim 10^{-1}$, four-orders of magnitude larger than in the Earth. It is possible that the relatively stronger effect of advection relative to rotation in the Sun partially explains why the Sun has more periodic dynamics than the Earth.

6. Conclusion

We have observed the effect of Lorentz forces on turbulent flow by applying large external fields to a flow in liquid sodium. An interaction parameter of $N = 17$ has been reached for magnetic Reynolds number up to $Re_m = 18$.

Our observations indicate five regimes, which reflect changes in the dynamics as Lorentz forces come to dominate. As the applied field increases, the turbulence is suppressed and the system undergoes first an $m = 1$ instability (with smooth walls only) and then an $m = 2$ instability. From magnetic data and comparison to Hollerbach and Skinner (2001), we infer that the instabilities consist of precessing columnar vortices aligned with the field (we have no direct velocity or vorticity data). The induced field patterns are divided into zones at different polar angles. The number of zones grows with increasing interaction parameter. The precession speed of these patterns increases with imposed field in regime III, and then remains approximately constant with imposed field in regime IV. This increasing precession speed may result from the shortening of the poloidal wavelength of the inferred vortices, possibly related to the mechanism described in Labbé et al. (1996). When this wavelength is comparable to the sphere radius, equatorially anti-symmetric states result.

The torque needed to co-rotate the impellers changes with interaction parameter, and depends non-trivially on the topography of the spherical vessel. These results might be useful in future studies of core–mantle coupling. Our results also suggest that in the absence of global rotation, at large interaction parameter, core–mantle coupling is insensitive to the mantle topography.

Acknowledgements

This work was funded by the NSF Grants EAR-0116129, EAR-0207789, and DMR-9896037. We gratefully acknowledge assistance from Alfred Cawthorne, James Drake, Khurrum Gillani, Donald Martin, Edward Ott, Nicholas Peffley, John Rodgers, James Stone, Santiago Triana, and Daniel Zimmerman. We benefited greatly from helpful comments by two anonymous referees. D.P. Lathrop is a Cottrell Scholar of the Research Corporation.

References

Aldridge, K.D., Bloxham, J., Gubbins, D., Hide, R., Hinderer, J., Hutcheson, K.A., Jault, D., Jones, C.A., Legros, H., Le Mouël, J.-L, Lloyd, D., Wahr, J.M., Whaler, K.A., Zhang, K., 1990. Core–mantle interactions. Sur. Geophys. 11, 329–353.

Alemany, A., Moreau, R., Sulem, L., Firsch, U., 1979. Influence of an external magnetic field on homogenous turbulence. J. de Méca. 18, 277–313.

Beckley, H., Colgate, S., Ferrel, R., Romero, V., Westphahl, D., 1998. Fluid flow for an experimental $\alpha - \Omega$ dynamo: plume rotation. Bull. Am. Phys. Soc. 2057, 43.

Bloxham, J., Gubbins, D., 1987. Thermal core–mantle interactions. Nature 325, 511–513.

Brito, D., Cardin, P., Nataf, H.-C., Marolleau, G., 1995. An experiment study of a geostropic vortex of gallium in a transverse magnetic field. Phys. Earth Planet Inter. 91, 77–98.

Brito, D., Cardin, P., Nataf, H.-C., Olson, P., 1996. Experiments on Joule heating and the dissipation of energy in the Earth's core. Geophys. J. Int. 127, 339–347.

Busse, F.H., 2000. Homogeneous dynamos in planetary cores and in the laboratory. Annu. Rev. Fluid Mech. 32, 383–408.

Charbonneau, P., MacGregor, K.B., 1997. Solar interface dynamos. II. Linear, kinematic models in spherical geometry. Astrophys. J. 486, 502–520.

Christensen-Dalsgaard, J., et al., 1996. The current state of solar modeling. Science 272, 1286–1292.

Constable, C.G., Johnson, C.L., Lund, S.P., 2000. Global geomagnetic field models for the past 3000 years: transient or permanent flux lobes? Proc. R. Soc. Lon. A 358, 991–1008.

Cowling, T.G., 1957. Magnetohydrodynamics. Interscience, New York, 115 pp.

Dormy, E., Valet, J.-P., Courtillot, V., 2000. Numerical models of the geodynamo and observation constraints. Geochem. Geophys. Geosys. 1, 2000GC000062.

Dudley, M.L., James, R.W., 1989. Time-dependent kinematic dynamos with stationary flows. Proc. R. Soc. Lon. A 425, 407–429.

Fisher, G.H., Fan, Y., Longcope, D.W., Linton, M.G., Pevtsov, A.A., 2000. The solar dynamo and emerging flux. Sol. Phys. 192, 119–139.

Gilman, P.A., 2000. Fluid dynamics and MHD of the solar convection zone and tachocline: current understanding and unsolved problems. Sol. Phys. 192, 27–48.

Gailitis, A., Lielausis, O., Dement'ev, S., Platacis, E., Cifersons, A., Gerbeth, G., Gundrum, T., Stefani, F., Christen, M., Hanel, H., Will, G., 2000. Detection of a flow induced magnetic field eigenmode in the Riga dynamo facility. Phys. Rev. Lett. 84, 4365–4368.

Gailitis, A., Lielausis, O., Platacis, E., Dement'ev, S., Cifersons, A., Gerbeth, G., Gundrum, T., Stefani, F., Christen, M., Will, G., 2001. Magnetic field saturation in the Riga dynamo experiment. Phys. Rev. Lett. 86, 3024–3027.

Glatzmaier, G.A., Roberts, P.H., 1995. A three-dimensional self-consistent computer simulation of a geomagnetic field reversal. Nature 377, 203–209.

Gough, D.O., McIntyre, M.E., 1998. Inevitability of a magnetic field in the Sun's radiative interior. Nature 394, 755–757.

Gubbins, D., Bloxham, J., 1987. Morphology of the geomagnetic field and implications for the geodynamo. Nature 325, 509–511.

Hollerbach, R., Skinner, S., 2001. Instabilities of magnetically induced shear layers and jets. Proc. R. Soc. Lon. A 457, 785–802.

Hulot, G., Eymin, C., Langlais, B., Mandea, M., Olsen, N., 2002. Small-scale structure of the geodynamo inferred from Oersted and Magsat satellite data. Nature 416, 620–623.

Jault, J., Hulot, J.L., Le Mouël, J.L., 1996. Mechanical core–mantle coupling and dynamo modelling. Phys. Earth Planet Inter. 98, 187–191.

Kays, W.M., Crawford, M.E., 1980. Convective heat and mass transfer. McGraw-Hill, New York, 420 pp.

Kuang, W., Bloxham, J., 1997. An Earth-like numerical dynamo model. Nature 389, 371–374.

Labbé, R., Pinton, J.-F., Fauve, S., 1996. Study of the von Kármán flow between coaxial corotating disks. Phys. Fluids 8, 914–922.

Lehnert, B., 1955. An instability of laminar flow of mercury caused by an external magnetic field. Proc. R. Soc. Lon. A 233, 299–302.

Moffatt, H.K., 1978. Magnetic Field Generation in Electrically Conducting Fluids. Cambridge University Press, Cambridge, 343 pp.

Moreau, R., 1990. Magnetohydrodynamics. Kluwer Academic Publishers, Dordrecht, 313 pp.

O'Connell, R., Kendrik, R., Nornberg, M., Spence, E., Bayliss, A., Forest, C.B., 2001. On the possibility of a homogeneous dynamo in the laboratory. In: Chossat, P., Armbruster, D., Oprea, I. (Eds.), Proceedings of the NATO Advanced Research Workshopon Dynamo and Dynamics: a Mathematical Challenge, vol. 66. Kluwer Academic Publishers, Cargèse, France, pp. 59–66.

Odier, P., Pinton, J-.F., Fauve, S., 1998. Advection of a magnetic field by a turbulent swirling flow. Phys. Rev. E 58, 7397–7401.

Peffley, N.L., Cawthorne, A.B., Lathrop, D.P., 2000. Toward a self-generating dynamo: the role of turbulence. Phys. Rev. E 61, 5287–5294.

Roberts, P.H., 1988. Future of geodynamo theory. Geophys. Astrophys. Fluid Dyn. 44, 3–31.

Roberts, P.H., Glatzmaier, G.A., 2000. Geodynamo theory and simulations. Rev. Mod. Phys. 72, 1081–1123.

Steenbeck, M., Krause, F., Rädler, K.-H., 1966. A calculation of the mean electromotive force in an electrically conducting fluid in turbulent motion, under the influence of Coriolis forces. Z. Naturforsch. 21a, 369–376. [English Trans.: Roberts, P.H., Stix, M., 1971. The Turbulent Dynamo: A Translation of a Series of Papers by F. Krause, K.-H. Rädler, M. Steenbeck. Technical Note 60, NCAR, Boulder, CO, pp. 29–47.]

Stieglitz, R., Müller, U., 2001. Experimental demonstration of a homogeneous two-scale dynamo. Phys. Fluids 13, 561–564.